energies

MDPI

Article

A State-Space Model for Stability Boundary Analysis of Grid-Following Voltage Source Converters Considering Grid Conditions

Guodong Liu * and Michael Starke

Electrification and Energy Infrastructures Division, Oak Ridge National Laboratory, Oak Ridge, TN 37831, USA; starkemr@ornl.gov
* Correspondence: liug@ornl.gov; Tel.: +1-865-241-9732

Abstract

With the growing significance of renewable energy resources and energy storage systems, the number of grid-connected inverters has been rising at an increasingly rapid pace. Generally, these inverters are directly integrated with the distribution network by synchronizing with the grid voltage at the point of common coupling. However, the low grid strength and varying R/X ratios, as the common characteristics of most distribution networks or weak grids, can lead to dynamic interactions that comprise stability and limit the power transfer capacity of grid-connected inverters. To ensure stable operation of the inverters, researchers must determine the stability boundary, described as the maximum power transfer capacity of grid-connected inverters under the premise of maintaining system small-signal stability. For this purpose, we propose to formulate a state-space model of the system in the synchronously rotating dq-frame of reference and perform eigenvalue analysis to determine the stability boundary. With a detailed model of the control structure and parameters of the grid-connected inverters, the stability boundary is identified as a surface with respect to different grid strengths and R/X ratios. Case study results of proposed eigenvalue analysis are compared with those of admittance model-based stability analysis as well as time-domain simulation using a switching model in Matlab/Simulink, validating the effectiveness and accuracy of the proposed eigenvalue analysis for stability boundary identification.

Keywords: state-space model; stability boundary; grid-connected inverters; maximum power transfer capacity; weak grid

1. Introduction

Driven by competitive cost, a massive increase in global manufacturing, and emerging markets worldwide, photovoltaic (PV) technology has emerged as dominant for the expansion of global electricity generation, representing more than 50% of all newly installed electricity generating capacity since 2022 [1]. In 2024, around 38 GW of PV was deployed in the US, representing 61% of the country's newly installed electricity generating capacity [2]. In states such as California and Nevada, more than 30% of electricity consumption is generated by PV [3]. A vast number of energy storage systems (ESSs) have also been installed as supporting facilities for mitigating fluctuations of PV generation and ensuring reliable power supply [4]. Although some of these PV and energy storage devices are operating off-grid, the majority are connected to utility grids by numerous inverters, ranging from residential projects of several kilowatts to industrial parks of several megawatts.

Academic Editor: Mario Marchesoni

Received: 20 February 2026
Revised: 14 March 2026
Accepted: 16 March 2026
Published: 19 March 2026

The PV and ESS inverters are designed primarily as grid-following voltage source converters (VSCs), which act as current sources that synchronize with the grid voltage and frequency at the point of common coupling (PCC) using a phase-lock loop (PLL) to inject or absorb power [5]. The stable operation of grid-following VSCs requires a stable grid voltage and frequency, presenting challenges for weak grids or off-grid operation. Unfortunately, most PVs are directly integrated into low-voltage distribution networks with low grid strength, sometimes even at the terminal or edge of the distribution grid with very weak grid connection owing to affordability of land [6]. Determining the stability boundary of the grid-following VSCs is of significant importance to ensure their stable operation.

Early work in inverter stability analysis established the importance of small-signal stability assessment based on the eigenanalysis of the system state-space model in the time domain and impedance/admittance model-based methods in the frequency domain [7,8]. Among them, the state-space model-based methods in the time domain account for the most. By linearizing the system dynamics around an equilibrium operating point obtained via power flow calculation, the small-signal state-space model of the system at the equilibrium operating point is established. Subsequently, system stability is assessed by analyzing the eigenvalue distribution of the state matrix of the system state-space model [9]. Depending on whether the inner current loops, PLL dynamics, outer droop or voltage control loops, and static/dynamic distribution network are being considered, various state-space models are formulated with different complex levels reflected by the dimensions of the state matrix. A computationally efficient 5-th order electromagnetic model representing the inverter as a droop-controlled AC voltage source is employed to assess the stability of islanded microgrids in [10–12]. This model ignores the inner current loops and PLL dynamics while focusing on network dynamics; thus, it is efficient for stability assessment of microgrids with a large number of inverters. The inner current control loops and inverter LC/LCL filter are incorporated into the state-space model in [13,14]. However, in weak grids, the interaction between the PLL and the high grid impedance can introduce instability, leading to subsynchronous oscillations and loss of synchronization. For this reason, the PLL dynamics are considered in the formulated state-space model in [15,16]. Nevertheless, grid impedance is ignored in [15] and simply modeled as static state in [16], which cannot accurately show the effects of grid strength on the stability of inverters.

Full knowledge of controller design and grid configuration is required to build an accurate VSC state-space model. In reality, this might be challenging because of incomplete inverter information and varying grid conditions. On the contrary, the impedance model could be applied to black-box systems (with unknown control design or system configuration) through measured impedance and the Generalized Nyquist Criterion to assess stability of the system at the PCC [17]. For a white-box system, the impedance model-based method could also lead to accurate prediction of system stability [18]. More importantly, the small-signal stability of the system could be improved by reshaping the output impedance of the VSCs through modification of the control algorithm. Thus, the stability range of the system could be expanded [19,20]. Similarly, in [21], a virtual impedance is introduced into the controller to enhance stability and improve the maximum power transfer capacity of grid-connected VSCs in weak grids. Despite these advantages, reports indicate that determinant-based Nyquist criterion can potentially result in incorrect stability analysis results with pure inductance models in the multi-input–multi-output (MIMO) model because of the introduction of imaginary axis poles [22]. In [23], an equivalent single-input–single-output open-loop transfer function is formulated based on the MIMO model of grid-connected VSCs, thereby enabling the application of a Nyquist curve for analyzing system stability.

Existing work has emphasized that the stability of grid-following VSCs heavily depends on grid strength, which should be accurately modeled in the small-signal state-space model. Nevertheless, the R/X ratio of the grid impedance, which also plays a crucial role in determining the damping of power oscillations, is often ignored. To ensure stable operation, the formulated state-space model of grid-following VSCs must explicitly consider both grid strength and the R/X ratio. Furthermore, to determine the stability boundary of the grid-following VSCs with accuracy, the formulation of a state-space model should be expanded to include detailed representations of inner current loops, outer droop or voltage control loops, PLL dynamics, and filter effects. In view of this gap, we formulate the state-space model of a grid-connected VSC explicitly considering the grid strength, R/X ratio, and detailed control strategy and parameters of the converters. Then, eigenanalysis is performed on the state matrix of the formulated state-space model to identify the stability boundary of the grid-connected VSC and investigate the effects of these factors on the stability boundary. The effectiveness of the state-space model and eigenvalue analysis is validated by comparing the results with those of admittance model-based stability analysis and time-domain simulation using a switching model in Matlab/Simulink R2024b. The main contributions of this paper are as follows:

1. Develop a state-space model of a grid-connected VSC that accounts not only for the converter control strategy and parameters and the grid strength, but also for the R/X ratio and the dynamics of the grid impedance, enabling a comprehensive stability analysis;
2. Identify the stability boundary of grid-connected VSC as a surface in the space of grid strength and R/X ratio, and present an explicit, analytically tractable framework for computing the boundary;
3. Validate the effectiveness and accuracy of the proposed eigenvalue analysis for stability boundary identification through comparison with the results of admittance model-based stability analysis and time-domain simulation using a switching model in Matlab/Simulink, providing multiple, complementary interpretations of the stability boundary derivation from different perspectives.

It should be noted that the modeling framework is an incremental yet practically useful refinement of established state-space approaches, rather than an introduction of fundamentally new stability concepts or converter physics. Our contributions lie primarily in: (i) a more comprehensive formulation and derivation of a stability boundary that accounts for the R/X ratio and the dynamic model of grid impedance; (ii) an explicit, analytically tractable framework for computation of the boundary; and (iii) multiple, complementary interpretations of the stability-boundary derivation from different perspectives.

The rest of this paper is outlined as follows: Section 2 presents the state-space model of the grid-connected VSC, whereas the admittance model-based stability analysis in the frequency domain is introduced in Section 3. Simulation validation is presented in Section 4, and the paper is concluded in Section 5.

2. State-Space Model of Grid-Connected Converter System

2.1. System Configuration

Figure 1 illustrates a PV inverter connected to an AC grid. As can be seen, the resistance, inductance, and capacitance of the inverter filter are denoted by R_f, L_f, and C_f, respectively. The equivalent resistance and inductance of the grid are denoted by R_g and L_g, respectively. Grid strength, characterized by the short-circuit ratio (SCR), is defined as (1) [24]. This is the ratio of short-circuit capacity of the AC grid at the PCC (S_{AC}) to the capacity of the PV inverter (S_N). If the SCR is less than 3, the AC grid is generally seen as a weak grid.

https://doi.org/10.3390/en19061521

Furthermore, larger grid impedance (e.g., long distribution feeder) leads to a weaker grid (i.e., smaller SCR).

$$SCR = \frac{S_{AC}}{S_N} = \frac{V_{pcc}^2}{Z_g S_N}. \quad (1)$$

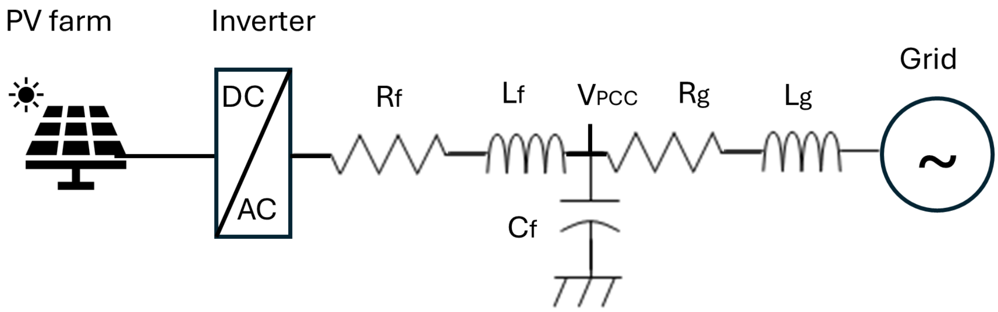

Figure 1. A PV inverter connected to an AC grid.

2.2. Controller Design

Figure 2 illustrates the topology of a three-phase VSC connected to the grid, represented by an ideal voltage source u_g and the grid impedances R_g and L_g. The output voltage and current of the VSC are denoted by u_c and i_c, respectively, whereas the voltage and current at the PCC are denoted by u_o and i_o, respectively. To avoid low-frequency passive resonance, the filter capacitor $C_f \approx 0$. Subsequently, $i_o \approx i_c$.

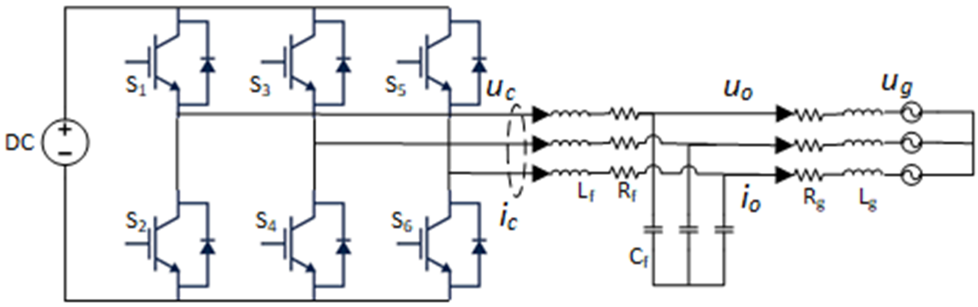

Figure 2. Topology of a three-phase VSC connected to the grid.

Figure 3 illustrates the control diagram of the grid-following VSC. As can be seen, the controller consists of a PLL, an inner current control loop, and an outer active power and voltage magnitude control loop. The aim of the controller is to deliver the specified active power (P^*) to the PCC while maintaining the voltage magnitude at the PCC as specified (V_o^*).

The grid-following VSCs are designed to synchronize with the grid at the PCC by tracking the voltage phase angle at the PCC (θ_o) through the PLL. Ideally, the output angle of PLL (θ_{pll}) should lock with θ_o in real time; thus, the controller *d*-*q* frame overlaps with the system *d*-*q* frame perfectly. However, the PLL cannot be perfect but instead is subject to limited accuracy due to time delay and other factors; this leads to a small misalignment between the system *d*-*q* frame and the control *d*-*q* frame (see Figure 4). For easy distinction, the variables in the controller *d*-*q* frame are indicated with the superscript *ctrl*.

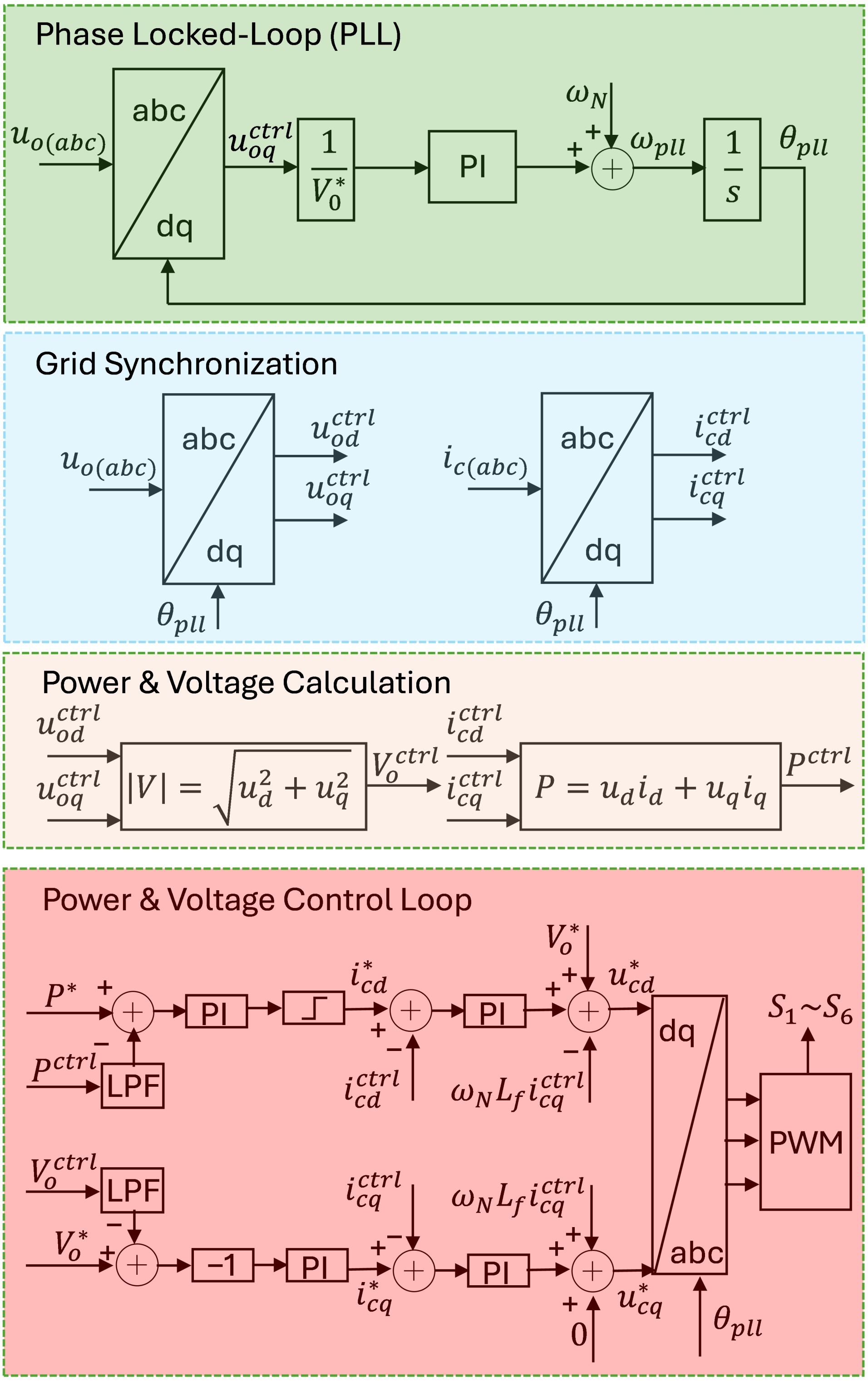

Figure 3. Control diagram of grid-following VSC.

2.3. Steady-State Operating Point

To formulate the state-space model, we need to determine the steady-state operating point, around which the system is linearized. For this purpose, we need to conduct a steady-state power flow study on the equivalent circuit of the AC grid connected to the PCC of the VSC, as illustrated in Figure 5.

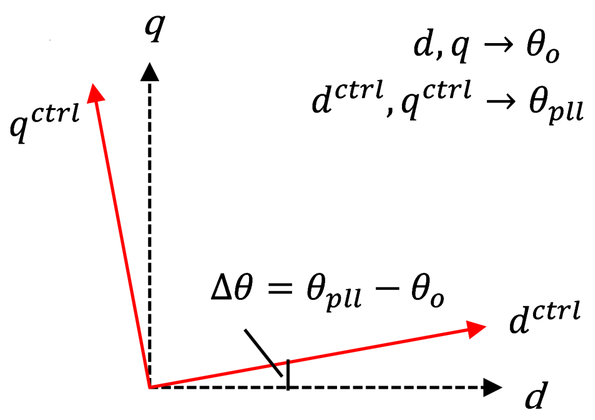

Figure 4. Controller *d*-*q* frame and system *d*-*q* frame.

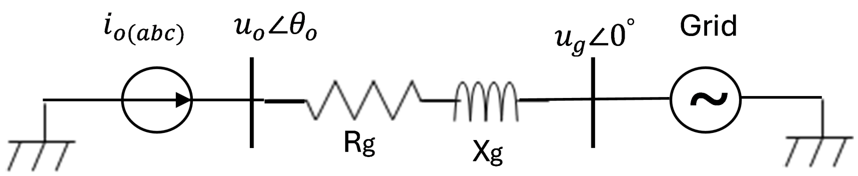

Figure 5. Equivalent circuit of the AC grid.

The steady-state power flow equations of the equivalent circuit of the AC grid are presented in (2) and (3). Given a specified active power requirement and the maintained constant magnitude of the voltage at the PCC, the corresponding phase angle θ_o at the PCC could be calculated according to (2). Subsequently, the reactive power Q^* needed for maintaining constant voltage magnitude at the PCC could be solved by simply substituting θ_o into (3).

$$P^* = \frac{V_o^*}{R_g^2 + X_g^2}\left[R_g\left(V_o^* - V_g cos\theta_o\right) + X_g V_g sin\theta_o\right]. \tag{2}$$

$$Q^* = \frac{V_o^*}{R_g^2 + X_g^2}\left[X_g\left(V_o^* - V_g cos\theta_o\right) - R_g V_g sin\theta_o\right]. \tag{3}$$

Considering the capacity limit of the VSC, if the solved $Q^* \geq \sqrt{S^2 - P^{*2}}$, then Q^* is limited to be $\sqrt{S^2 - P^{*2}}$, indicating the specified constant voltage magnitude at the PCC cannot be maintained. To boost this voltage, the active power has to be reduced by limiting the current reference i_{cd}, as shown in Figure 3. With P^* ,Q^*, and θ_o, the initial steady-state operating point in the corresponding *d*-*q* frame—e.g., u_{od0}, u_{oq0}, i_{od0}, and i_{oq0}—could be obtained [15].

2.4. State-Space Model

In essence, the state-space model is a group of linearized differential equations that describe the system and the controller at the steady state operating point. The inverter filter and the grid impedance in the system *d*-*q* frame are presented as (4)–(6), which are linear differential equations.

$$\begin{cases} L_g \frac{di_{od}}{dt} = u_{od} - u_{gd} - R_g i_{od} + \omega L_g i_{oq} \\ L_g \frac{di_{oq}}{dt} = u_{oq} - u_{gq} - R_g i_{oq} - \omega L_g i_{od} \end{cases}. \tag{4}$$

$$\begin{cases} C_f \frac{du_{od}}{dt} = i_{cd} - i_{od} + \omega C_f u_{oq} \\ C_f \frac{du_{oq}}{dt} = i_{cq} - i_{oq} - \omega C_f u_{od} \end{cases}. \tag{5}$$

$$\begin{cases} L_f \frac{di_{cd}}{dt} = u_{cd} - u_{od} - R_f i_{cd} + \omega L_f i_{cq} \\ L_f \frac{di_{cq}}{dt} = u_{cq} - u_{oq} - R_f i_{cq} - \omega L_f i_{cd} \end{cases}. \quad (6)$$

Considering the misalignment between the system *d*-*q* frame and the control *d*-*q* frame, the variables described in the system *d*-*q* frame need to transform into corresponding ones described in the controller *d*-*q* frame, according to (7).

$$\begin{bmatrix} u_{od}^{ctrl} \\ u_{oq}^{ctrl} \end{bmatrix} = \begin{bmatrix} cos\left(\theta_{pll} - \theta_o\right) & sin\left(\theta_{pll} - \theta_o\right) \\ -sin\left(\theta_{pll} - \theta_o\right) & cos\left(\theta_{pll} - \theta_o\right) \end{bmatrix} \begin{bmatrix} u_{od} \\ u_{oq} \end{bmatrix}. \quad (7)$$

Because the error of θ_{pll} has to be small if the system is stable, we can assume $\theta_{pll} \approx \theta_o$. Consequently, (7) could be linearized as (8) with a further assumption of $cos\left(\theta_{pll} - \theta_o\right) \approx 1$ and $sin\left(\theta_{pll} - \theta_o\right) \approx \theta_{pll} - \theta_o$.

$$\begin{cases} \triangle u_{od}^{ctrl} = \triangle u_{od} + u_{oq0} \triangle \theta_{pll} \\ \triangle u_{oq}^{ctrl} = \triangle u_{oq} - u_{od0} \triangle \theta_{pll} \end{cases}. \quad (8)$$

Similarly, we can derive variables i_{cd}^{ctrl}, i_{cq}^{ctrl}, u_{cd}^{ctrl}, and u_{cd}^{ctrl} in the controller *d*-*q* frame as linear expressions in (9) and (10).

$$\begin{cases} \triangle i_{cd}^{ctrl} = \triangle i_{cd} + i_{cq0} \triangle \theta_{pll} \\ \triangle i_{cq}^{ctrl} = \triangle i_{cq} - i_{cd0} \triangle \theta_{pll} \end{cases}. \quad (9)$$

$$\begin{cases} \triangle u_{cd}^{ctrl} = \triangle u_{cd} + u_{cq0} \triangle \theta_{pll} \\ \triangle u_{cq}^{ctrl} = \triangle u_{cq} - u_{cd0} \triangle \theta_{pll} \end{cases}. \quad (10)$$

Regarding the VSC controller, the inner current control loop is presented by linear differential Equation (11).

$$\begin{cases} \frac{d\int i_d}{dt} = i_{cd}^{*} - i_{cd}^{ctrl} \\ \frac{d\int i_q}{dt} = i_{cq}^{*} - i_{cq}^{ctrl} \end{cases}, \quad (11)$$

where the integrators of current in the *d*-axis and *q*-axis are denoted by $\int i_d$ and $\int i_q$, separately. Consequently, the reference output voltages of the VSC in the *d*-axis and *q*-axis are represented as (12).

$$\begin{cases} u_{cd}^{*} = Kp\_i_d(i_{cd}^{*} - i_{cd}^{ctrl}) + Ki\_i_d \cdot \int i_d - \omega L_f i_{cq}^{ctrl} + V_o^{*} \\ u_{cq}^{*} = Kp\_i_q(i_{cq}^{*} - i_{cq}^{ctrl}) + Ki\_i_q \cdot \int i_q - \omega L_f i_{cd}^{ctrl} + 0 \end{cases}. \quad (12)$$

Similar to the inner current control loop, the outer active power and PCC voltage control loop is presented as linear differential Equation (13).

$$\begin{cases} \frac{d\int P}{dt} = P^{*} - P_{LPF}^{ctrl} \\ \frac{d\int V_o}{dt} = (-1)\left(V_o^{*} - V_{oLPF}^{ctrl}\right) \end{cases}, \quad (13)$$

where the integrators of active power and voltage magnitude at the PCC are denoted by $\int P$ and $\int V_o$, separately. In addition, the active power and magnitude of voltage at the PCC after passing the low-pass filter (LPF) are denoted by P_{LPF}^{ctrl} and V_{oLPF}^{ctrl}, respectively. The outputs of the outer active power and PCC voltage control loop are the reference currents in the d-axis and q-axis, separately, represented as (14).

$$\begin{cases} i_{cd}^{*} = Kp\_P(P^{*} - P_{LPF}^{ctrl}) + Ki\_P \cdot \int P \\ i_{cq}^{*} = Kp\_V_o(-1)(V_o^{*} - V_{oLPF}^{ctrl}) + Ki\_V_o \cdot \int V_o \end{cases}. \tag{14}$$

The active power and magnitude of voltage at the PCC are formulated in (15), then linearized as represented in (16). At the steady state operating point, u_{od}^{ctrl} and u_{oq}^{ctrl} are equal to $V_o^{*}$and 0, respectively.

$$\begin{cases} P^{ctrl} = u_{od}^{ctrl} i_{cd}^{ctrl} + u_{oq}^{ctrl} i_{cq}^{ctrl} \\ V_o^{ctrl} = \sqrt{\left(u_{od}^{ctrl}\right)^2 + \left(u_{oq}^{ctrl}\right)^2} \end{cases}. \tag{15}$$

$$\begin{cases} \triangle P^{ctrl} = \triangle u_{od}^{ctrl} i_{cd0}^{ctrl} + \triangle u_{oq}^{ctrl} i_{cq0}^{ctrl} + V_o^{*} \triangle i_{cd}^{ctrl} \\ \triangle V_o^{ctrl} = \triangle u_{od}^{ctrl} \end{cases} \tag{16}$$

The LPFs for the active power and magnitude of voltage at the PCC are described by linear differential Equation (17), where ω_{LPF} is the cut-off angular frequency of the LPF.

$$\begin{cases} \frac{dP_{LPF}^{ctrl}}{dt} = \omega_{LPF}\left(P^{ctrl} - P_{LPF}^{ctrl}\right) \\ \frac{dV_{oLPF}^{ctrl}}{dt} = \omega_{LPF}\left(V_o^{ctrl} - V_{oLPF}^{ctrl}\right) \end{cases}. \tag{17}$$

According to Figure 3, the PLL of the VSC could be described by linear differential Equation (18).

$$\begin{cases} \frac{d\int u_{oq}}{dt} = \frac{u_{oq}^{ctrl}}{V_o^{*}} \\ \frac{d\theta_{pll}}{dt} = Kp\_pll\frac{u_{oq}^{ctrl}}{V_o^{*}} + Ki\_pll \cdot \int u_{oq} + \omega_N \end{cases}. \tag{18}$$

Based on the differential Equations (4)–(6), (11), (13), (17) and (18), the state-space model of the grid-following VSC could be formulated and simply expressed as Equation (19).

$$\triangle \dot{x}_{14\times1} = A_{14\times14} \cdot \triangle x_{14\times1} + B_{14\times2} \cdot \triangle u_{2\times1}, \tag{19}$$

as $\triangle x_{14\times1} = \left[\triangle i_{od}, \triangle i_{oq}, \triangle u_{od}, \triangle u_{oq}, \triangle i_{cd}, \triangle i_{cq}, \triangle \int i_d,\ \triangle \int i_q, \triangle \int P, \triangle \int V_o, \triangle \int u_{oq}, \triangle\theta_{pll}, \triangle P_{LPF}^{ctrl},\ \triangle V_{oLPF}^{ctrl}\right]$. The eigenvalue of the state matrix $A_{14\times14}$ indicates the small-signal stability of the grid-following VSC.

2.5. Linearization Assumptions and Applicability Limits

Note that the linearized expressions in (8)–(10) are based on the assumption that the error of θ_{pll} is small (i.e., $\theta_{pll} \approx \theta_o$) when the system is stable. Under this assumption, we approximate $cos\left(\theta_{pll} - \theta_o\right)$ and $sin\left(\theta_{pll} - \theta_o\right)$ as 1 and $\theta_{pll} - \theta_o$, respectively. During normal operation of a grid-following VSC, the PLL phase error θ_{pll} is generally very low. In a stable, stiff, or mildly weak grid with minimal harmonic distortion, the steady-state phase tracking error is usually negligible (nearly 0°). A PLL phase error of less than 5° to 10° is generally considered tolerable for maintaining stable steady-state operation [25]. PLL phase errors larger than 10° typically induce active power and voltage oscillations and may lead to VSC instability.

For a PLL phase error of 10°, we can get $cos\left(\theta_{pll} - \theta_o\right) = 0.9848$ and $sin\left(\theta_{pll} - \theta_o\right) = 0.1737$. Compared with their approximations of 1 and $\theta_{pll} - \theta_o = 0.1745$, the relative errors are 1.5% and 0.5%, respectively. Therefore, the linearization assumptions are sufficiently accurate for small-signal stability analysis.

During transient stability events, such as grid faults that cause significant voltage dips at the PCC, the PLL phase error may exceed critical thresholds (often around 10° to 20° in weak grid studies). In such cases, the PLL may fail to track the grid angle, potentially leading to VSC tripping, as observed in large-scale PV disconnection events. The proposed small-signal state-space model is not applicable under these large-disturbance conditions.

It should also be noted that the PV-side is modeled as an ideal DC source (stiff DC, as shown in Figure 2) in this paper. Under this assumption, the PV parameters do not appear dynamically in the small-signal model and therefore cannot introduce oscillatory modes or lead to instability. However, if the PV-side is modeled as dynamic DC link with capacitors, then PV-side dynamics might influence stability by changing the DC-link operating point, introducing additional DC-side states and coupling control between DC and AC side, etc. Generally, PV-side parameters can affect stability indirectly, but in a grid-following VSC the dominant small-signal stability mechanisms are typically governed by: (i) grid strength (grid impedance), (ii) PLL dynamics, and (iii) inner current-loop and outer power- and voltage-loop dynamics.

3. Admittance Model of Grid-Connected Converter System

Like the small-signal state-space model, the admittance model is also based on the linearized model of the system at the equilibrium operating point, although in the frequency domain. The small-signal linearized expressions of the VSC filter and the grid impedance in the frequency domain are presented as (4)–(6).

$$\begin{bmatrix} \triangle u_{od} \\ \triangle u_{oq} \end{bmatrix} = \begin{bmatrix} \triangle u_{gd} \\ \triangle u_{gq} \end{bmatrix} + \begin{bmatrix} sL_g + R_g & -\omega L_g \\ \omega L_g & sL_g + R_g \end{bmatrix} \begin{bmatrix} \triangle i_{od} \\ \triangle i_{oq} \end{bmatrix}. \tag{20}$$

$$\begin{bmatrix} \triangle i_{cd} \\ \triangle i_{cq} \end{bmatrix} = \begin{bmatrix} \triangle i_{od} \\ \triangle i_{oq} \end{bmatrix} + \begin{bmatrix} sC_f & -\omega C_f \\ \omega C_f & sC_f \end{bmatrix} \begin{bmatrix} \triangle u_{od} \\ \triangle u_{oq} \end{bmatrix}. \tag{21}$$

$$\begin{bmatrix} \triangle u_{cd} \\ \triangle u_{cq} \end{bmatrix} = \begin{bmatrix} \triangle u_{od} \\ \triangle u_{oq} \end{bmatrix} + \begin{bmatrix} sL_f + R_f & -\omega L_f \\ \omega L_f & sL_f + R_f \end{bmatrix} \begin{bmatrix} \triangle i_{cd} \\ \triangle i_{cq} \end{bmatrix}. \tag{22}$$

According to Equation (18), the small signal linearized expression of PLL in the frequency domain could be presented as (23). By substituting (23) into (8), $\triangle\theta_{pll}$ can be derived as a function of $\triangle u_{oq}$, as stated in (24).

$$\triangle\theta_{pll} = \left(Kp\_pll + \frac{Ki\_pll}{s}\right)\frac{\triangle u_{oq}^{ctrl}}{sV_o^*}. \tag{23}$$

$$\triangle\theta_{pll} = \frac{Kp\_pll \cdot s + Ki\_pll}{s^2 + Kp\_pll \cdot s + Ki\_pll} \cdot \frac{1}{V_o^*} \cdot \triangle u_{oq} = \frac{G_{pll}}{V_o^*} \cdot \triangle u_{oq}. \tag{24}$$

By substituting (24) into (8), (9), and (10), and in the meantime setting $u_{od0} = V_o^*$ and $u_{oq0} = 0$, we can get $\triangle u_{od}^{ctrl}$, $\triangle u_{oq}^{ctrl}$, $\triangle i_{cd}^{ctrl}$, $\triangle i_{cq}^{ctrl}$, $\triangle u_{cd}^{ctrl}$, and $\triangle u_{cq}^{ctrl}$ in the frequency domain as (25), (26) and (27), respectively.

$$\begin{bmatrix} \triangle u_{od}^{ctrl} \\ \triangle u_{oq}^{ctrl} \end{bmatrix} = \begin{bmatrix} \triangle u_{od} \\ \triangle u_{oq} \end{bmatrix} - \begin{bmatrix} 0 & 0 \\ 0 & G_{pll} \end{bmatrix} \begin{bmatrix} \triangle u_{od} \\ \triangle u_{oq} \end{bmatrix}. \tag{25}$$

$$\begin{bmatrix} \triangle i_{cd}^{ctrl} \\ \triangle i_{cq}^{ctrl} \end{bmatrix} = \begin{bmatrix} \triangle i_{cd} \\ \triangle i_{cq} \end{bmatrix} - \begin{bmatrix} 0 & -\frac{i_{cq0}}{V_o^*} \cdot G_{pll} \\ 0 & \frac{i_{cd0}}{V_o^*} \cdot G_{pll} \end{bmatrix} \begin{bmatrix} \triangle u_{od} \\ \triangle u_{oq} \end{bmatrix}. \tag{26}$$

$$\begin{bmatrix} \triangle u_{cd}^{ctrl} \\ \triangle u_{cq}^{ctrl} \end{bmatrix} = \begin{bmatrix} \triangle u_{cd} \\ \triangle u_{cq} \end{bmatrix} - \begin{bmatrix} 0 & -\frac{u_{cq0}}{V_o^*} \cdot G_{pll} \\ 0 & \frac{u_{cd0}}{V_o^*} \cdot G_{pll} \end{bmatrix} \begin{bmatrix} \triangle u_{od} \\ \triangle u_{oq} \end{bmatrix}. \tag{27}$$

For the inner current control loop, (12) could be represented in the frequency domain as (28).

$$\begin{bmatrix} \triangle u_{od}^* \\ \triangle u_{oq}^* \end{bmatrix} = \begin{bmatrix} G_{pi-i_d} & 0 \\ 0 & G_{pi-i_q} \end{bmatrix} \cdot \left(\begin{bmatrix} \triangle i_{cd}^* \\ \triangle i_{cq}^* \end{bmatrix} - \begin{bmatrix} \triangle i_{cd}^{ctrl} \\ \triangle i_{cq}^{ctrl} \end{bmatrix} \right) + \begin{bmatrix} 0 & -\omega L_f \\ \omega L_f & 0 \end{bmatrix} \begin{bmatrix} \triangle i_{cd}^{ctrl} \\ \triangle i_{cq}^{ctrl} \end{bmatrix}, \tag{28}$$

where $G_{pi-i_d} = Kp\_i_d + Ki\_i_d/s$, and $G_{pi-i_q} = Kp\_i_q + Ki\_i_q/s$.

Similarly, the outer active power and PCC voltage control loop could be represented as (29).

$$\begin{bmatrix} \triangle i_{cd}^* \\ \triangle i_{cq}^* \end{bmatrix} = \begin{bmatrix} G_{pi-P} & 0 \\ 0 & -G_{pi-V} \end{bmatrix} \cdot \left(\begin{bmatrix} \triangle P^* \\ \triangle V_o^* \end{bmatrix} - \begin{bmatrix} \triangle P_{LPF}^{ctrl} \\ \triangle V_{oLPF}^{ctrl} \end{bmatrix} \right), \tag{29}$$

where $G_{pi-P} = Kp\_P + Ki\_P/s$ and $G_{pi-V} = Kp\_V + Ki\_V/s$.

The small signal expressions of $\triangle P^{ctrl}$ and $\triangle V_o^{ctrl}$ in (16) are reformulated into matrix form as given in (30).

$$\begin{bmatrix} \triangle P^{ctrl} \\ \triangle V_o^{ctrl} \end{bmatrix} = \begin{bmatrix} i_{cd0}^{ctrl} & i_{cq0}^{ctrl} \\ 1 & 0 \end{bmatrix} \begin{bmatrix} \triangle u_{od}^{ctrl} \\ \triangle u_{oq}^{ctrl} \end{bmatrix} + \begin{bmatrix} V_o^* & 0 \\ 0 & 0 \end{bmatrix} \begin{bmatrix} \triangle i_{cd}^{ctrl} \\ \triangle i_{cq}^{ctrl} \end{bmatrix}. \tag{30}$$

For the LPFs of active power and magnitude of voltage at the PCC, (17) could be represented in the frequency domain as (31), where $G_{LPF} = \omega_{LPF}/(s + \omega_{LPF})$.

$$\begin{bmatrix} \triangle P_{LPF}^{ctrl} \\ \triangle V_{oLPF}^{ctrl} \end{bmatrix} = \begin{bmatrix} G_{LPF} & 0 \\ 0 & G_{LPF} \end{bmatrix} \begin{bmatrix} \triangle P^{ctrl} \\ \triangle V_o^{ctrl} \end{bmatrix}. \tag{31}$$

Now, we denote the 2by2 matrices in (20), (21) and (22) as B_{Lg}, B_{Cf}, and B_{Lf}, respectively; in (25), (26) and (27) as B_{pll-uo}, B_{pll-ic}, and B_{pll-uc}, respectively; in (28) and (29) as B_{pi-i}, B_{comp}, and B_{pi-PV}, respectively; and in (30) and (31) as B_i, B_u, and B_{LPF}, respectively. Subsequently, the equivalent small-signal control diagram of the grid-following VSC shown in Figure 3 could be established as that shown in Figure 6.

The small-signal control diagram of the grid-following VSC could be used to derive the equivalent admittance $Y(s)$ of the VSC and the equivalent impedance $Z_g(s)$ of the grid, as shown in Figure 6. Using $\triangle i_{cdq}$ and $\triangle u_{odq}$ as the input and output, respectively, the equivalent grid impedance $Z_g(s)$ is obtained as in (32). In addition, using $\triangle u_{odq}$ and $-\triangle i_{cdq}$ as the input and output, respectively, the equivalent admittance $Y(s)$ of the VSC could be obtained as in (33).

$$Z_g(s) = (B_{Lg}^{-1} + B_{Cf})^{-1}. \tag{32}$$

$$\begin{aligned} Y(s) \quad = \quad & (B_{Lf} + B_{pi-i} - B_{comp} + B_{pi-i} B_{pi-PV} B_{LPF} B_u)^{-1} \\ & \Big[B_{pi-i} B_{pi-PV} B_{LPF} B_i (I - B_{pll-uo}) + I - B_{pll-uc} \\ & -(B_{pi-i} - B_{comp} + + B_{pi-i} B_{pi-PV} B_{LPF} B_u) B_{pll-ic} \Big] \end{aligned} . \tag{33}$$

Given $Z_g(s)$ and $Y(s)$, the two eigenvalues of the 2by2 matrix $Y(s)Z_g(s)$ could be solved at every frequency, and the generalized Nyquist diagram could be drawn. Subsequently, the stability of the system could be assessed by the Generalized Nyquist Criterion [26].

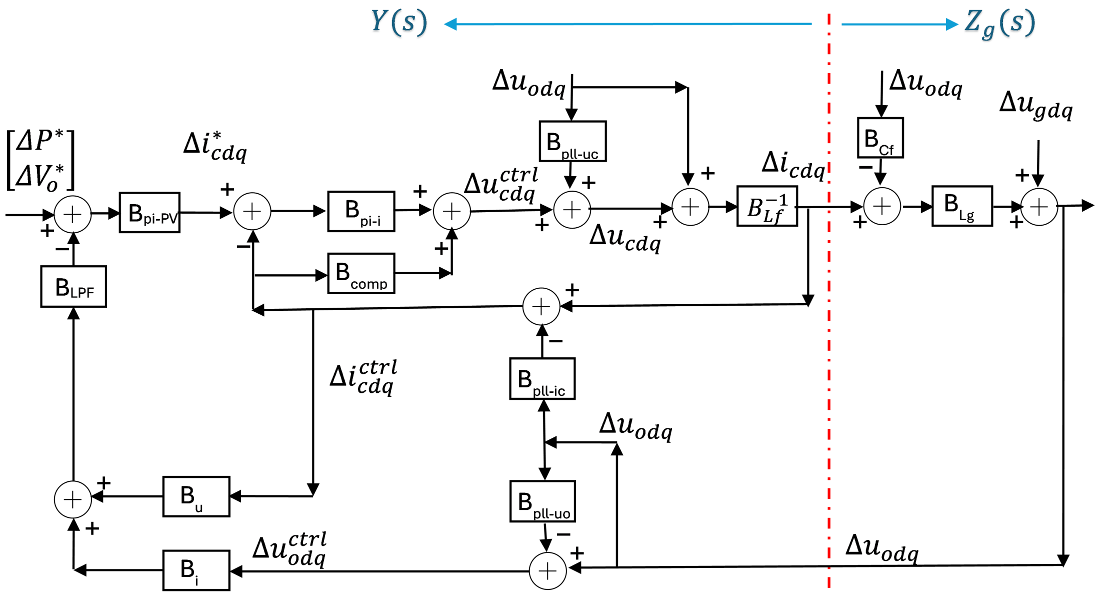

Figure 6. Small-signal control diagram of grid-following VSC.

4. Case Studies

4.1. Test System

A 500 kVA grid-following VSC is used for various case studies to examine the accuracy of the proposed eigenvalue analysis-based stability boundary identification and admittance model-based stability analysis. The parameters of the VSC and the grid are listed in Table 1. With these settings, the SCR is around 1.5, indicating a weak grid. The R/X ratio is about 0.01, indicating an inductive grid.

Table 1. Parameters of grid-following VSC and grid.

Parameter	Value
VSC capacity	500 kVA
Grid voltage/frequency	380 V/50 Hz
Output filter capacitance	100 µF
Output filter inductance/resistance	0.5 mH/0.5 mΩ
Grid resistance/inductance	0.2 mΩ/0.6 mH
Real power control loop $(Kp\_P,\ Ki\_P)$	(0.0114, 1.1429)
Voltage magnitude control loop $(Kp\_V_o,\ Ki\_V_o)$	(2, 100)
Inner current control loop $(Kp\_i_d/i_q,\ Ki\_i_d/i_q)$	(2, 200)
PLL $(Kp\_pll,\ Ki\_pll)$	(50, 1500)
ω_{LPF}	200 rad/s

Note that the parameters (including control parameters) of the VSC and the grid are mostly adopted from [16]. The control parameters were tuned in [16] to achieve the target closed-loop bandwidth and phase margin. The LPF parameters are taken from [8]. This work focuses on formulating a state-space small-signal model and performing eigenvalue analysis to determine whether a given operating point is stable. Detailed tuning methods for a grid-following VSC under weak-grid conditions can be found in [27].

4.2. Eigenvalue Analysis

By varying the active power at the PCC from 300 to 400 kW, the eigenvalue locus is shown in Figure 7a. The ends of the eigenvalue locus—i.e., the eigenvalues of the system when the PCC power is 400 kW—are plotted as red circles. Some of the eigenvalues start to appear on the right half plane when the PCC power is higher than 360 kW, indicating the system is losing small-signal stability. Thus, the stability boundary of the grid-following VSC under grid condition $SCR = 1.5$ and $R/X = 0.01$ is obtained (i.e., P_{PCC} = 360 kW).

By repeating this process under a different SCR and R/X ratio, the stability boundary of a grid-connected VSC with respect to grid strength (i.e., SCR) and R/X ratio could be obtained as a surface, as shown in Figure 7b. The maximum transferred power at the PCC is highest with large SCR and small R/X ratio (i.e., a strong inductive grid condition). Under an inductive grid condition (i.e., small R/X ratio), the maximum power transferred at the PCC decreases as the SCR gets smaller, meaning the stability boundary shrinks under weaker grid conditions. Note that the maximum transferred power at the PCC is close to corresponding power received at the grid side, meaning the power loss is small. As the R/X ratio increases (i.e., the grid becomes resistive), the maximum power transferred at the PCC increases as the SCR gets smaller, meaning the stability boundary expands under the weaker grid condition due to the damping effect of the grid resistance R_g. A large gap is present between the maximum transferred power at the PCC and the corresponding power received at the grid side, meaning the power loss is significant owing to the large grid resistance R_g. In fact, the corresponding power received at the grid side changes to negative, meaning the grid side also sends power to the PCC. These results indicate the importance of considering the R/X ration in analyzing the maximum power transfer capability of grid-following VSC.

All eigenvalues of state matrix $A_{14\times14}$ under the condition of $SCR = 1.5$, $R/X = 0.01$, and P_{PCC} = 350 kW are presented in Table 2. As shown, the system exhibits 10 modes in total, comprising 4 oscillatory modes and 6 non-oscillatory (real) damping modes. Under this condition, all eigenvalues lie in the left-half complex plane, indicating that the system is stable. The dominant (largest real-part) eigenvalue is λ_{12}.

Table 2. Eigenvalues of state matrix $A_{14\times14}$ with $SCR = 1.5$, $R/X = 0.01$, and P_{PCC} = 350 kW.

Mode	Eigenvalue	Oscillation Frequency (Hz)
λ_1, λ_2	$-33.17 \pm j6229.53$	5.28
λ_3, λ_4	$-1129.65 \pm j5566.67$	179.79
λ_5	-3596.24	0
λ_6	-1591.16	0
λ_7, λ_8	$-351.44 \pm j71.09$	55.93
λ_9	-88.11	0
$\lambda_{10}, \lambda_{11}$	$-19.71 \pm j32.35$	3.14
λ_{12}	-17.20	0
λ_{13}	-45.56	0
λ_{14}	-52.07	0

https://doi.org/10.3390/en19061521

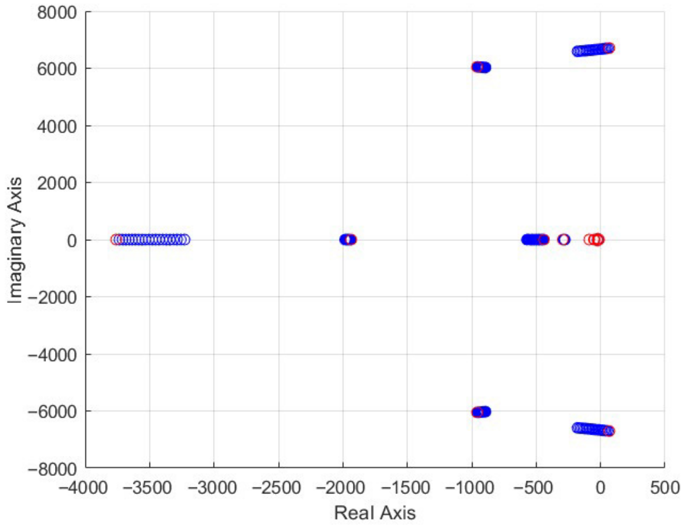

(**a**) Eigenvalue locus

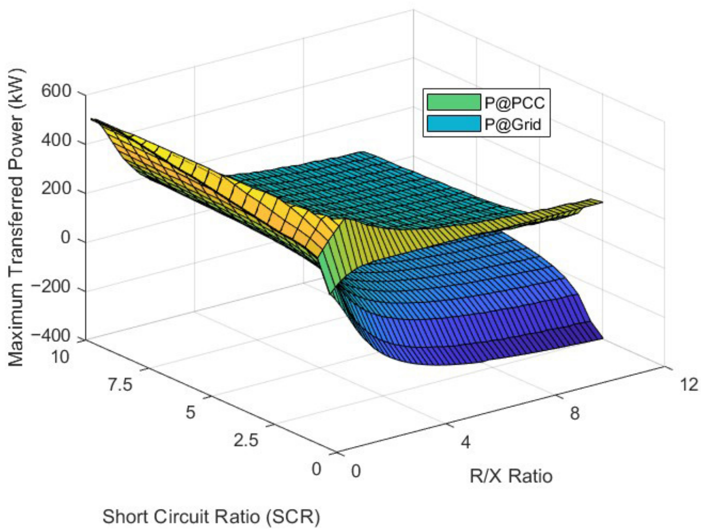

(**b**) Stability boundary

Figure 7. Eigenvalue locus and stability boundary calculated by eigenvalue analysis of a state-space model.

To identify the parameters that may lead to system instability, the participation factors of the state variables for each mode identified in Table 2 are calculated and presented in Table 3. The state variables with the largest participation in each mode are identified and highlighted in red. For the mode with largest eigenvalue λ_{12}, the dominant participating state variables are associated with PCC voltage magnitude control. This indicates that PCC voltage magnitude control is a major contributor to reduced stability under the specified conditions. The PLL is strongly associated with modes λ_{10} and λ_{11}, which have the second-largest eigenvalues, suggesting that the PLL may also contribute to instability through these modes.

Table 3. Participation factors of state variables for each mode.

Variable	Participation Factor									
	λ_1, λ_2	λ_3, λ_4	λ_5	λ_6	λ_7, λ_8	λ_9	$\lambda_{10}, \lambda_{11}$	λ_{12}	λ_{13}	λ_{14}
i_{od}	0.1789	0.0054	0.0510	0.0127	0.2708	0.0054	0.0068	0.0199	0.0085	0
i_{oq}	0.0126	0.2299	0.0005	0.4006	0.0306	0.0007	0.0329	0.0133	0.0105	0.0088
u_{od}	0.4170	0.0156	0.0395	0	0.0030	0	0.0002	0	0	0
u_{oq}	0.0207	0.4575	0.0015	0.0623	0.0007	0	0	0.0001	0	0
i_{cd}	0.2133	0.0211	0.5091	0.0141	0.0090	0.0047	0.0001	0	0.0015	0
i_{cq}	0.0091	0.2371	0.0349	0.3297	0.0243	0.0006	0.0008	0.0014	0.0054	0
$\int i_d$	0.0001	0.0001	0.0120	0.0012	0.0041	0.0047	0.0026	0.0010	0.199	0.6606
$\int i_q$	0	0.0015	0.0008	0.0221	0.0045	0.0115	0.0190	0.0059	0.6171	0.2414
$\int P$	0.0022	0.0002	0.0085	0.0004	0.0235	0.8788	0.0096	0.0086	0.0588	0.0573
$\int V_o$	0	0	0.0003	0.0022	0.0339	0.0029	0.0585	0.8008	0.0290	0.0051
$\int u_{oq}$	0	0	0	0.0012	0.0010	0.0020	0.4019	0.0689	0.0389	0.0077
θ_{pll}	0.00050	0.0141	0.0007	0.0664	0.01166	0.0039	0.4548	0.0294	0.0202	0.0056
P_{LPF}^{ctrl}	0.1419	0.0130	0.3154	0.0083	0.1321	0.0823	0.0017	0.0006	0.0094	0.0096
V_{LPF}^{ctrl}	0.0031	0.0038	0.0250	0.0781	0.4502	0.0017	0.0107	0.0494	0.0007	0

To show the necessity of modeling the grid impedance in a dynamic state as proposed in this work, the state-space model presented in [16], which simply models the grid impedance in steady-state only by ignoring its dynamics, is also employed to identify the stability boundary (as shown in Figure 8a). The differences compared with the results of the proposed model are shown in Figure 8b. Although the error is generally very small for most of the scenarios, it could be more than 20% under the scenario of small SCR and small R/X ratio (i.e., weak inductive grid condition). This indicates the necessity of modeling the grid impedance in a dynamic state, especially under weak inductive grid conditions.

It should be noted that the gain margins of the PI controller parameters cannot be inferred from Figures 7 and 8, since these figures show the stability boundary of the grid-connected VSC as a surface with respect to grid strength and the R/X ratio. Nevertheless, the proposed state-space model can be used to determine the PI gain margins by varying the PI gains while keeping all other parameters at their nominal values. This will be included in our future work.

4.3. Admittance Model-Based Stability Analysis

Figure 9a,b show the generalized Nyquist diagram of the matrix $Y(s)Z_g(s)$ with P_{PCC} = 300 kW and 400 kW, respectively. As shown in Figure 9a, (−1, 0) is not encircled, whereas the open-loop system has no zero in the right half plane, indicating small-signal stability with P_{PCC} = 300 kW. Meanwhile, in Figure 9b, (−1, 0) is encircled clockwise, whereas the open-loop system has no zero in the right half plane, indicating small-signal instability with P_{PCC} = 400 kW.

The generalized Nyquist diagram could be used to assess the stability of the system; however, examining the encirclement visually is challenging. For this reason, a more straightforward method for stability assessment based on the admittance model is presented in [28]. The system is stable if the characteristic polynomial has no zero in the right-half plane or if $det(I + Y(s)Z_g(s)) = 0$ should have all roots in the left-half plane. Using this method, the stability boundary of grid-connected VSC with respect to the grid strength (i.e., SCR) and R/X ratio could be obtained as a surface, as shown in Figure 10a. The stability boundary calculated based on the admittance model is compared with that obtained based on the eigenvalue analysis of the state-space model; the difference is shown in Figure 10b. As shown, the error is generally very small for all scenarios, an indication of the accuracy of admittance model-based stability analysis.

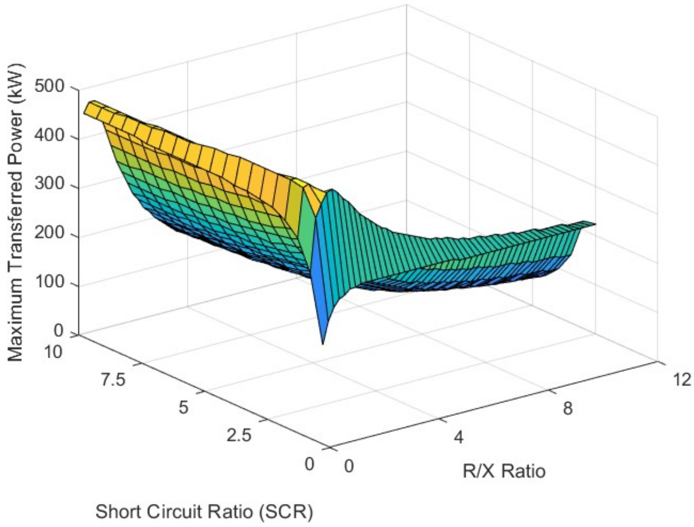

(**a**) Stability boundary

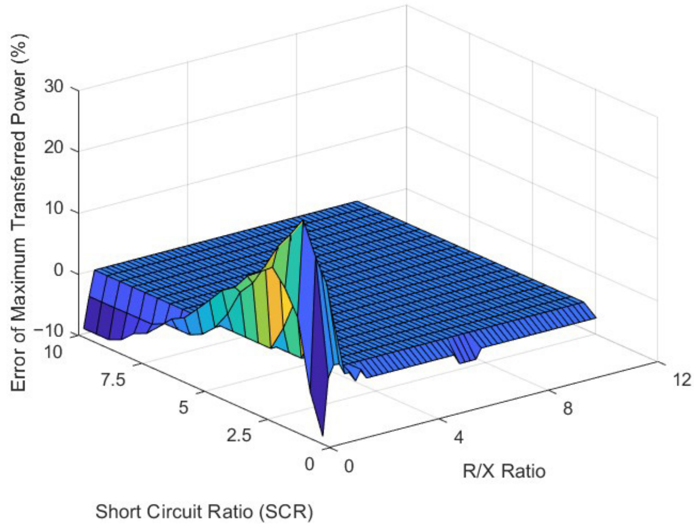

(**b**) Relative error

Figure 8. Calculated stability boundary and relative error by eigenvalue analysis of state-space model in [16].

4.4. Time-Domain Simulation Validation

The accuracy of the stability boundary determined by using the eigenvalue analysis of the state-space model is further validated by comparing with the results of a switch model-based simulation in Matlab/Simulink. Using the parameters in Table 1 and the control structure in Figure 3, the switch model of a grid-following VSC connected to the grid is built in Matlab/Simulink. The simulation results in various scenarios with different SCR and R/X ratio are shown in Figures 11–13. In specific, the simulation results of scenarios with different SCR and very low R/X ratios (i.e., R/X = 0.01, indicating an inductive grid) are shown in Figure 11, whereas those of scenarios with medium R/X ratio (i.e., R/X = 1)

https://doi.org/10.3390/en19061521

and high R/X ratio (i.e., R/X = 5, indicating a resistive grid) are shown in Figure 12 and Figure 13, respectively.

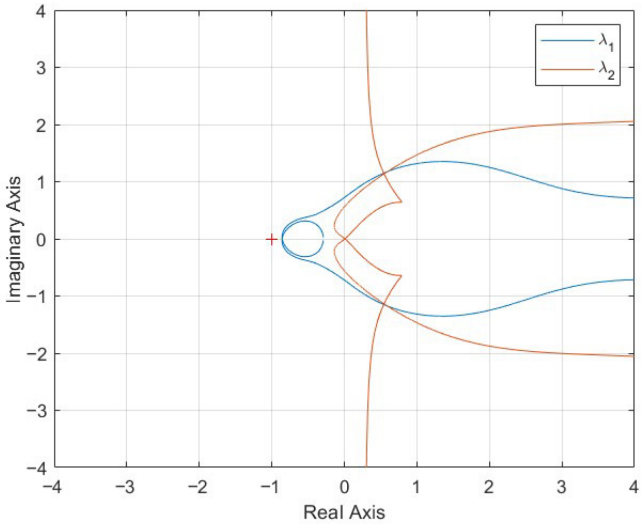

(**a**) P_{PCC} = 300 kW

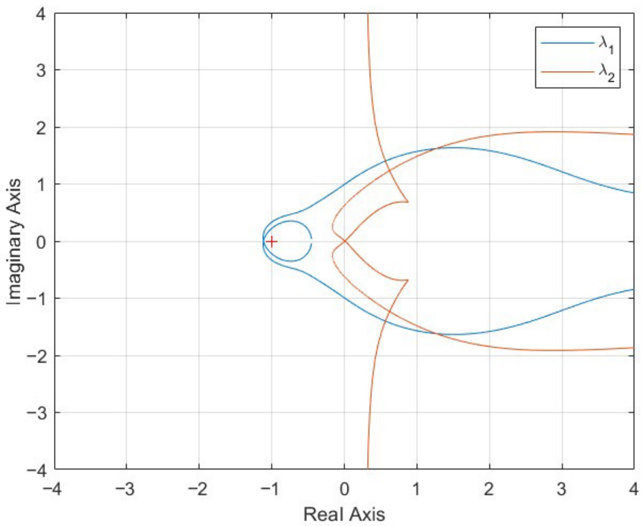

(**b**) P_{PCC} = 400 kW

Figure 9. Generalized Nyquist diagram by using the admittance model.

The maximum transferred powers obtained by the switch model simulation and by using the proposed eigenvalue analysis are compared in Table 4. The maximum transferred power calculated by using eigenvalue analysis are generally the same as or close to the corresponding ones obtained by switch model simulation, thereby demonstrating the effectiveness of the proposed eigenvalue analysis. It should be noted that the maximum transferred powers obtained by the switch model simulation are slightly lower than those obtained by using the proposed eigenvalue analysis, especially when the R/X ratio is very small. This is because the linearized state-space model based eigenvalue analysis ignores the harmonics and other nonlinearities, which could affect the stability in the switch model simulation.

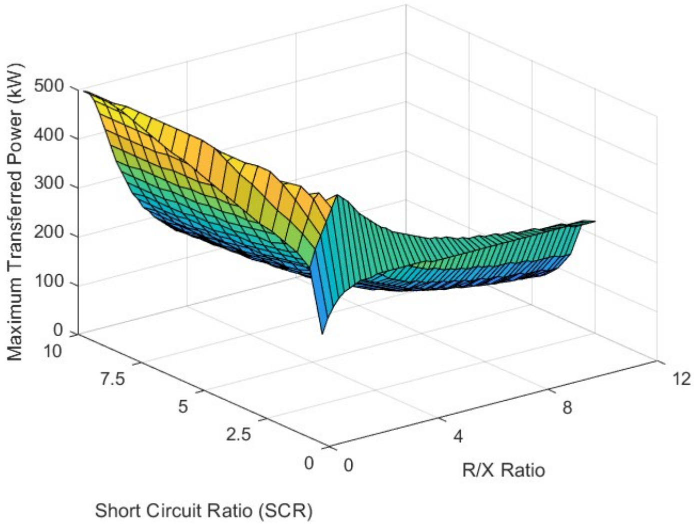

(**a**) Stability boundary

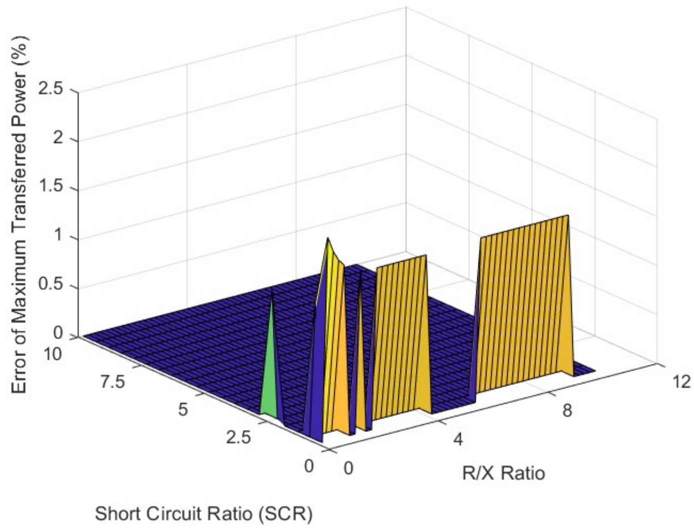

(**b**) Relative error

Figure 10. Calculated stability boundary and relative error by using admittance model-based stability analysis.

Table 4. Comparison of maximum transferred power by state-space model and switch model simulation.

Maximum Transferred Power by State-Space Model/Switch Model (kW)		**R/X Ratio**		
		0.01	**1**	**5**
SCR	1.5	360/340	450/450	255/255
	5	425/420	385/380	145/145
	10	495/480	370/370	120/120

As can be seen in Figure 11, the maximum transferred power of grid-following VSC is dominated by power stability of the system in the scenarios of small R/X ratio or neglectable grid resistance (i.e., R/X = 0.01). Owing to the small grid resistance, the reactive power required to keep constant PCC voltage is small, indicated by the small q-axis current i_{cq} at the PCC, as shown in Figure 11.

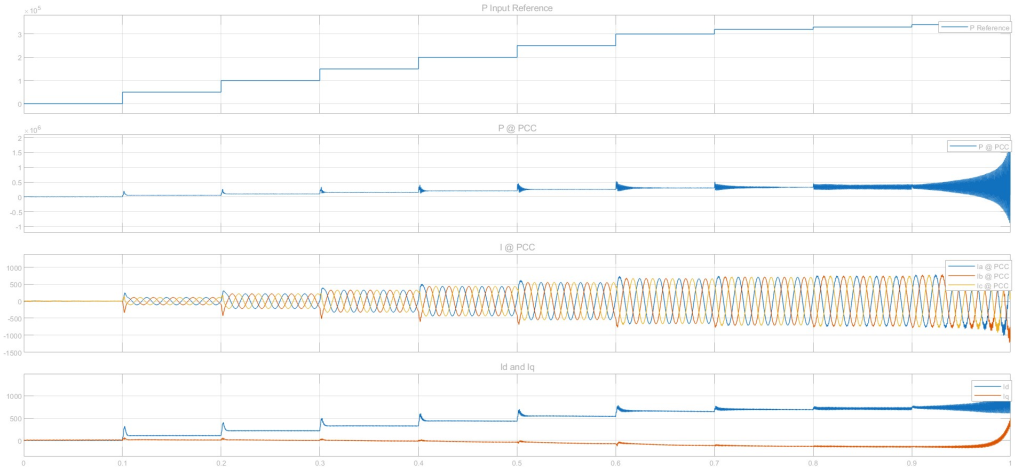

(**a**) SCR = 1.5 and R/X = 0.01

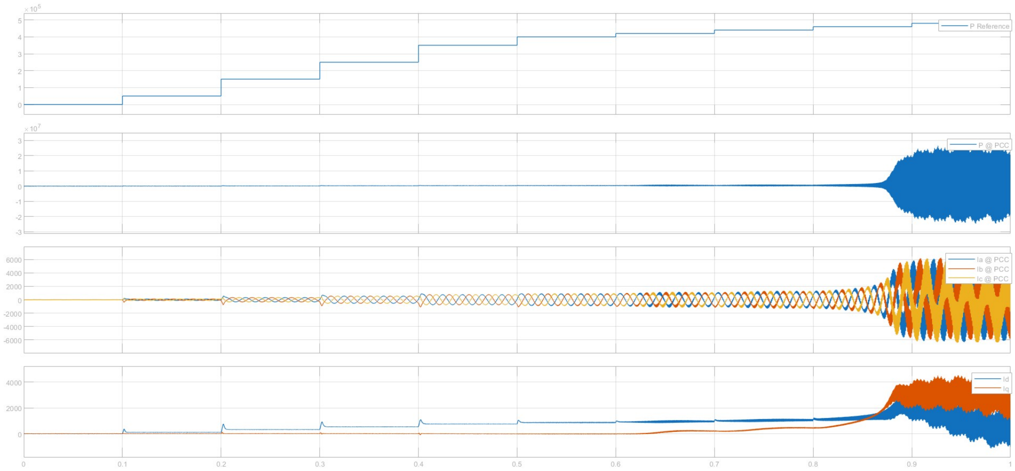

(**b**) SCR = 5 and R/X = 0.01

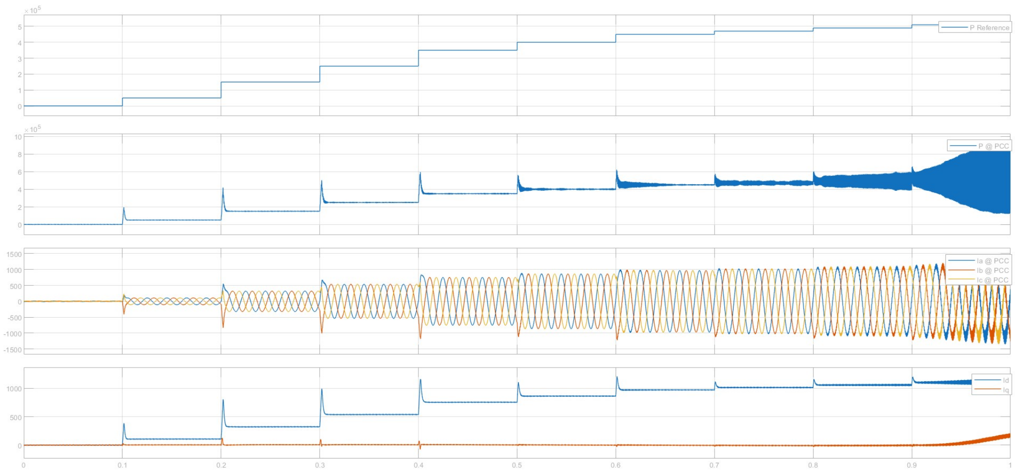

(**c**) SCR = 10 and R/X = 0.01

Figure 11. Simulation results of grid-following VSC under varying SCR and R/X = 0.01.

As the R/X ratio increases (e.g., R/X = 1, as shown in Figure 12), the increasing grid resistance improves the power stability of the system by enhancing the damping effect. Thus, power stability is no longer the dominating factor of the maximum transferred power of grid-following VSC. However, the increasing grid resistance requires certain reactive power to keep constant PCC voltage, indicated by the increased q-axis current i_{cq} at the PCC, as shown in Figure 12.

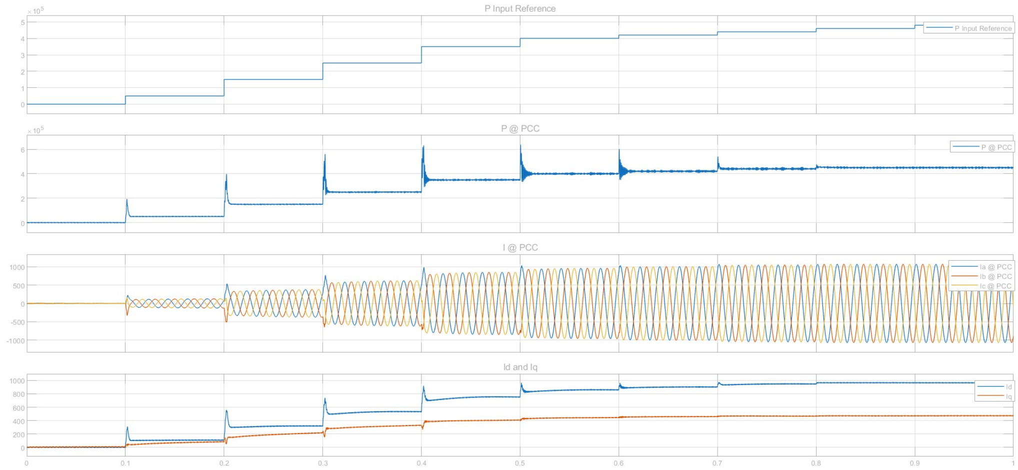

(**a**) SCR = 1.5 and R/X = 1

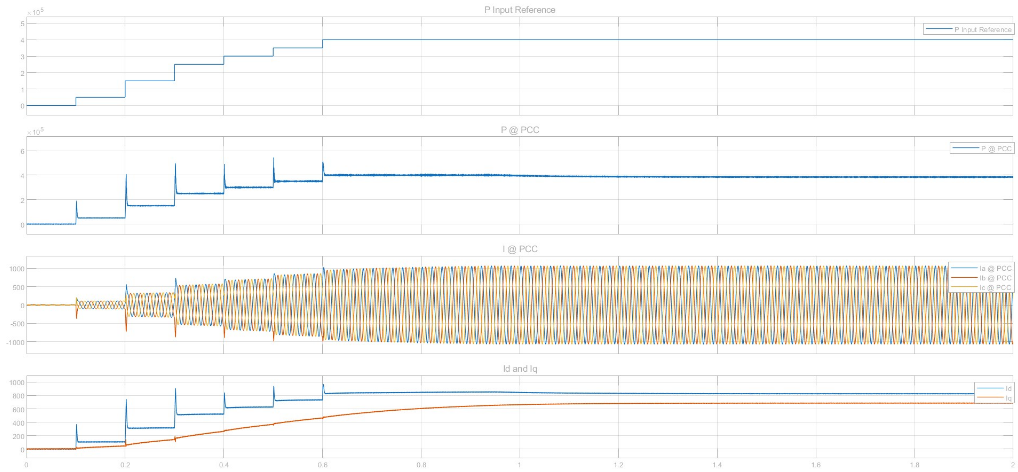

(**b**) SCR = 5 and R/X = 1

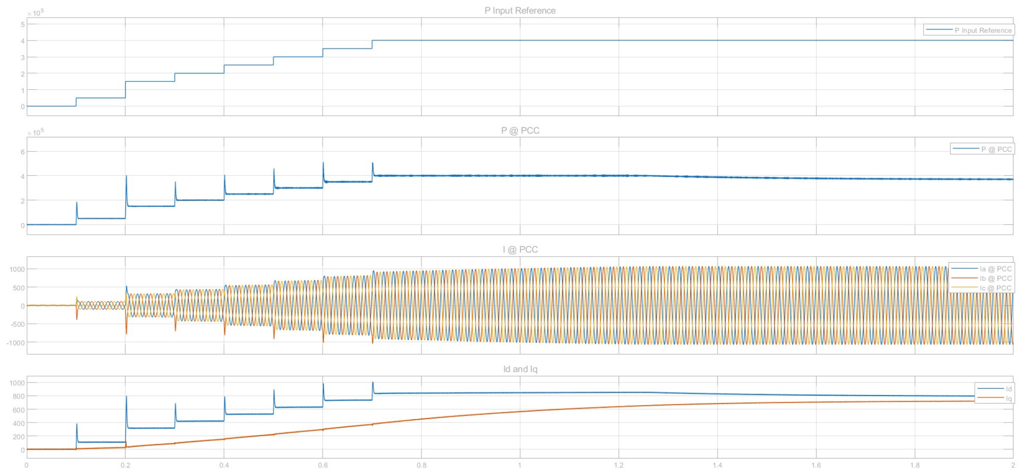

(**c**) SCR = 10 and R/X = 1

Figure 12. Simulation results of grid-following VSC under varying SCR and R/X = 1.

In the scenarios of resistive grid (e.g., R/X =5, as shown in Figure 13), significant reactive power is required to keep constant PCC voltage, indicated by the large q-axis current i_{cq} at the PCC. To maintain stable nominal voltage at the PCC, the active power at the PCC has to be reduced by limiting the d-axis current i_{cd}, due to the capacity limit of the converter. The limitation of the d-axis current i_{cd} could be easily observed in Figure 13b,c.

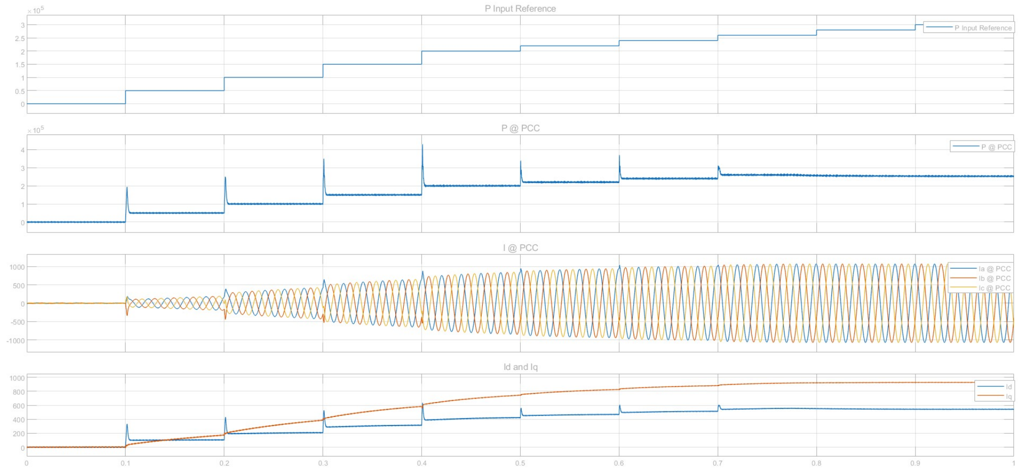

(**a**) SCR = 1.5 and R/X = 5

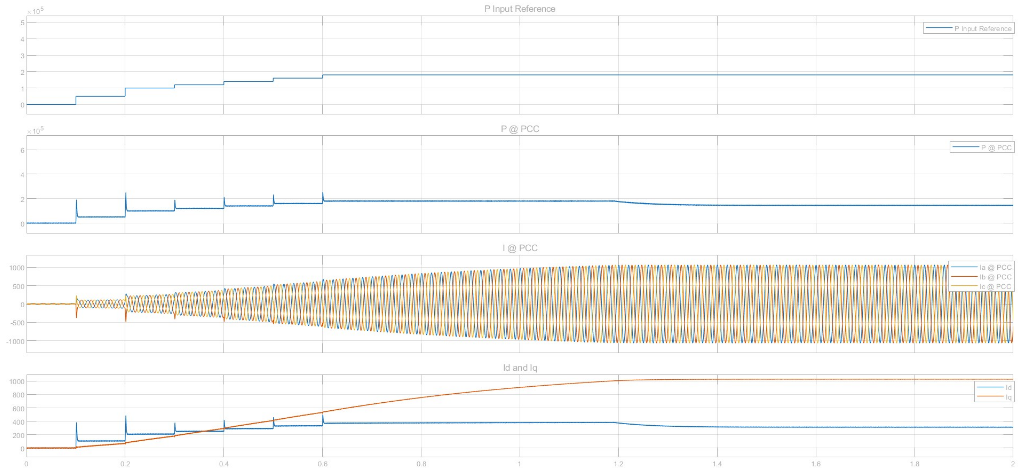

(**b**) SCR = 5 and R/X = 5

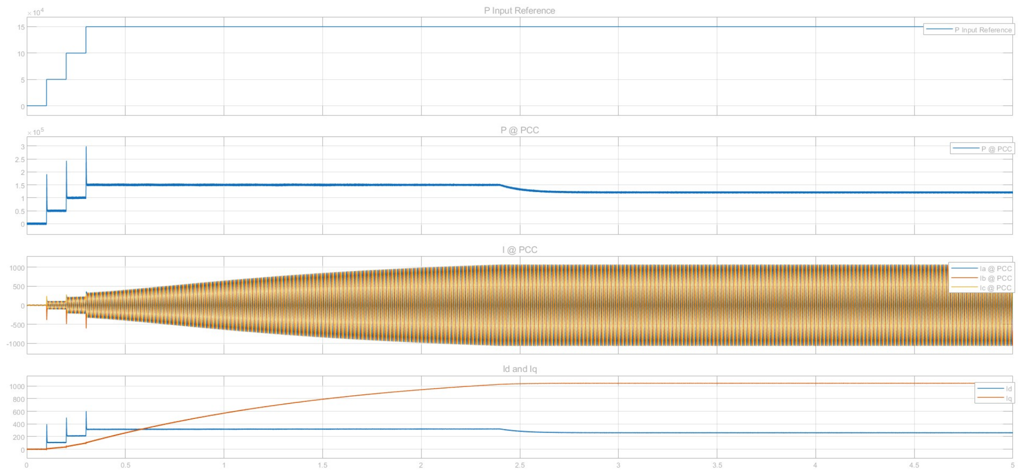

(**c**) SCR = 10 and R/X = 5

Figure 13. Simulation results of grid-following VSC under varying SCR and R/X = 5.

5. Conclusions

In this paper, we propose to identify the stability boundary of a grid-connected VSC by using state-space model-based eigenvalue analysis considering the detailed control structure and parameters of the VSC. The stability boundary is identified as a surface with respect to different grid strength and R/X ratios. The effectiveness and accuracy of the proposed eigenvalue analysis for stability boundary identification are validated by various case studies and a time-domain simulation using a switching model in Matlab/Simulink.

Considering the challenge of varying grid parameters in real-time applications, robust and adaptive control techniques that can dynamically react to grid parameter variability will be investigated in the future. Meanwhile, the PLL bandwidth, current controller gains and filter parameters also affect VSC stability. The resulting shift of the stability boundary with respect to individual parameters and combinations of these key parameters will be examined next. Moreover, the interplay between multiple inverters, interaction of their control loops, and the aggregated impact on grid stability will be explored.

Author Contributions: G.L. carried out the main research tasks and wrote the full manuscript. M.S. contributed to the development of the proposed methodology and provided important suggestions on writing of the paper. All authors have read and agreed to the published version of the manuscript.

Funding: This research was funded by US Department of Energy (DOE) Office of Electricity (OE) grant number 36590.

Data Availability Statement: The original contributions presented in the study are included in the article, further inquiries can be directed to the corresponding author.

Acknowledgments: Notice: This manuscript has been authored by UT-Battelle, LLC, under contract DE-AC05-00OR22725 with the US Department of Energy (DOE). The US government retains and the publisher, by accepting the article for publication, acknowledges that the US government retains a nonexclusive, paid-up, irrevocable, worldwide license to publish or reproduce the published form of this manuscript, or allow others to do so, for US government purposes. DOE will provide public access to these results of federally sponsored research in accordance with the DOE Public Access Plan (https://www.energy.gov/doe-public-access-plan, accessed on 1 January 2026).

Conflicts of Interest: The authors declare no conflicts of interest.

References

1. Haegel, N.M.; Kurtz, S.R. Global Progress Toward Renewable Electricity: Tracking the Role of Solar (Version 3). *IEEE J. Photovoltaics* **2023**, *13*, 768–776. [CrossRef]
2. Haegel, N.M.; Kurtz, S.R. Global Progress Toward Renewable Electricity: Tracking the Role of Solar (Version 5). *IEEE J. Photovoltaics* **2025**, *15*, 740–751. [CrossRef]
3. Ember. *US Electricity 2025 Special Report*; Ember: London, UK, 2025; pp. 1–20. Available online: https://ember-energy.org/app/uploads/2025/03/US-Electricity-2025-Special-Report.pdf (accessed on 10 March 2026).
4. International Energy Agency (IEA). *Batteries and Secure Energy Transitions*; IEA: Paris, France, 2024. Available online: https://www.iea.org/reports/batteries-and-secure-energy-transitions/ (accessed on 10 March 2026).
5. Gui, Y.; Wang, X.; Blaabjerg, F. Vector Current Control Derived from Direct Power Control for Grid-Connected Inverters. *IEEE Trans. Power Electr.* **2019**, *34*, 9224–9235. [CrossRef]
6. Blaabjerg, F.; Yang, Y.; Yang, D.; Wang, X. Distributed Power-Generation Systems and Protection. *Proc. IEEE* **2017**, *105*, 1311–1331. [CrossRef]
7. Xiong, L.; Liu, X.; Liu, Y.; Zhuo, F. Modeling and Stability Issues of Voltage-source Converter-Dominated Power Systems: A Review. *CSEE J. Power Energy Syst.* **2022**, *8*, 1530–1549.
8. Huang, L.; Wu, C.; Zhou, D.; Blaabjerg, F. Comparison of Three Small-Signal Stability Analysis Methods for Grid-Following Inverter. In Proceedings of the 2021 International Aegean Conference on Electrical Machines and Power Electronics (ACEMP) & 2021 International Conference on Optimization of Electrical and Electronic Equipment (OPTIM), Brasov, Romania, 2–3 September 2021; pp. 34–41.

9. Kong, L.; Xue, Y.; Qiao, L.; Wang, F. Review of Small-Signal Converter-Driven Stability Issues in Power Systems. *IEEE Open Access J. Power Energy* **2022**, *9*, 29–41. [CrossRef]
10. Vorobev, P.; Huang, P.-H.; Hosani, M.A.; Kirtley, J.L.; Turitsyn, K. High-Fidelity Model Order Reduction for Microgrids Stability Assessment. *IEEE Trans. Power Syst.* **2018**, *33*, 874–887. [CrossRef]
11. Manrique Machado, S.d.J.; da Silva, S.A.O.; Monteiro, J.R.B.d.A.; de Oliveira, A.A. Network Modeling Influence on Small-Signal Reduced-Order Models of Inverter-Based AC Microgrids Considering Virtual Impedance. *IEEE Trans. Smart Grid* **2021**, *12*, 79–92. [CrossRef]
12. Gorbunov, A.; Peng, J.C.-H.; Bialek, J.W.; Vorobev, P. Identification of Stability Regions in Inverter-Based Microgrids. *IEEE Trans. Power Syst.* **2022**, *37*, 2613–2623. [CrossRef]
13. Li, H.; Zhang, X.; Wan, T. Small-signal stability analysis of PV grid-connected inverter under weak-grid. In Proceedings of the 2019 6th International Conference on Information Science and Control Engineering (ICISCE), Shanghai, China, 20–22 December 2019; pp. 1141–1145.
14. Adib, A.; Mirafzal, B.; Wang, X.; Blaabjerg, F. On Stability of Voltage Source Inverters in Weak Grids. *IEEE Access* **2018**, *6*, 4427–4439. [CrossRef]
15. Alassaf, A.; Alsaleh, I.; Alateeq, A.; Alafnan, H. Grid-Following Inverter-Based Resource: Numerical State–Space Modeling. *Sustainability* **2023**, *15*, 8400. [CrossRef]
16. Jia, Q.; Yan, G.; Cai, Y.; Li, Y.; Zhang, J. Small-signal stability analysis of photovoltaic generation connected to weak AC grid. *J. Mod. Power Syst. Clean Energy* **2019**, *7*, 254–267. [CrossRef]
17. Wen, B.; Boroyevich, D.; Burgos, R.; Mattavelli, P.; Shen, Z. Small-Signal Stability Analysis of Three-Phase AC Systems in the Presence of Constant Power Loads Based on Measured d-q Frame Impedances. *IEEE Trans. Power Electr.* **2015**, *30*, 5952–5963. [CrossRef]
18. Fan, L.; Miao, Z. Admittance-Based Stability Analysis: Bode Plots, Nyquist Diagrams or Eigenvalue Analysis? *IEEE Trans. Power Syst.* **2020**, *35*, 3312–3315. [CrossRef]
19. Huang, L.; Wu, C.; Zhou, D.; Blaabjerg, F. A Simple Impedance Reshaping Method for Stability Enhancement of Grid-Following Inverter Under Weak Grid. In Proceedings of the 2021 IEEE 12th International Symposium on Power Electronics for Distributed Generation Systems (PEDG), Chicago, IL, USA, 28 June–1 July 2021; pp. 1–6.
20. Guerrero, J.M.; de Vicuna, L.G.; Matas, J.; Castilla, M.; Miret, J. Output impedance design of parallel-connected UPS inverters with wireless load-sharing control. *IEEE Trans. Ind. Electron.* **2005**, *52*, 1126–1135. [CrossRef]
21. Adib, A.; Fateh, F.; Mirafzal, B. Smart Inverter Stability Enhancement in Weak Grids Using Adaptive Virtual-Inductance. *IEEE Trans. Ind. Appl.* **2021**, *57*, 814–823. [CrossRef]
22. Qiao, L.; Xue, Y.; Kong, L.; Wang, F. A Potential Issue of Using the MIMO Nyquist Criterion in Impedance-Based Stability Analysis. *IEEE Open J. Power Electron.* **2022**, *3*, 899–904. [CrossRef]
23. Zhang, H.; Wang, X.; Harnefors, L.; Gong, H.; Hasler, J.P.; Nee, H.P. SISO Transfer Functions for Stability Analysis of Grid-Connected Voltage-Source Converters. *IEEE Trans. Ind. Appl.* **2019**, *55*, 2931–2941. [CrossRef]
24. Huang, L.; Wu, C.; Zhou, D.; Blaabjerg, F. Impact of Grid Strength and Impedance Characteristics on the Maximum Power Transfer Capability of Grid-Connected Inverters. *Appl. Sci.* **2021**, *11*, 4288. [CrossRef]
25. Fan, L.; Wang, Z.; Miao, Z. Large Angle Deviation in Grid-Following IBRs Upon Grid Voltage Dip. *IEEE Trans. Energy Convers.* **2024**, *39*, 368–378. [CrossRef]
26. Morris, J.F.; Ahmed, K.H.; Egea-Alvarez, A. Analysis of Controller Bandwidth Interactions for Vector-Controlled VSC Connected to Very Weak AC Grids. *IEEE J. Emerg. Sel. Top. Power Electron.* **2021**, *9*, 7343–7354. [CrossRef]
27. Li, C.; Wang, S.; Liang, J. Tuning Method of a Grid-Following Converter for the Extremely-Weak-Grid Connection. *IEEE Trans. Power Syst.* **2022**, *37*, 3169–3172. [CrossRef]
28. Morari, M.; Zafiriou, E. *Robust Process Control*; Prentice-Hall: Englewood Cliffs, NJ, USA, 1989.

https://doi.org/10.3390/en19061521